Proceedings of ASME Turbo Expo 2024
Turbomachinery Technical Conference and Exposition
GT2024
June 24-28, 2024, London, England, United Kingdom

GT2024-128243

LES Analysis of Loss Anomaly in a Turbine Blade with Large Trailing Edge Radius

Kenji Miki[1], Ali Ameri[1,2], Paul Giel[1,3]

[1]NASA Glenn Research Center, Cleveland, OH
[2]The Ohio State University, Columbus, OH
[3]HX5 LLC, NASA Glenn Research Center, Cleveland, OH

ABSTRACT

There is great interest in the usage of Ceramic Matrix Composites (CMC) as a turbine blade material. CMCs can tolerate higher temperatures than alloyed metallic blades, resulting in better thermal efficiency of gas turbine engines. However, depending on the manufacturing process of the CMC, blades may have a larger trailing edge thickness. The design space therefore needs to be updated due to the resulting flow physics. Recently, experimental results acquired at NASA Glenn Transonic Turbine Blade Cascade Rig showed that a loss measure generally increased with increasing trailing edge thickness. For one case however, the losses initially decreased with increasing Reynolds number, peaking at Re ~1.24×10^6, and then subsequently dropping to the original pre-peak trend. A possible cause of this intriguing phenomenon was speculated to be transonic vortex shedding, which is the mechanism of vortex shedding promoted by reflected shed pressure waves at the trailing edge at relatively high Reynolds numbers and higher Mach numbers. A Reynolds-averaged Navier-Stokes (RANS) analysis or a low-resolution large eddy simulation (LES) does not reproduce this apparent anomaly and thus it is worth performing a wall-resolved LES (the total mesh count of ~290 million cells) to investigate the aerodynamics of the CMC blade in the context of transonic vortex shedding. Our numerical results at Re=1,246,350 show that the pressure waves generated by the vortex shedding in the wake travel upstream and significantly influence the transition and separation on the suction side thus enhancing the said vortex shedding in the wake. This feedback seems not to hold under a low-Re condition (Re=621,900). The Reynolds number dependence was also examined by numerical perturbation of the pressure waves in the wake and by examining how such perturbation attenuates or endures. It is confirmed that the perturbation of the pressure waves is quickly damped.

Keywords: LES-LDKM, Free-stream turbulence, CMC, transonic vortex shedding

NOMENCLATURE

AUSM	Advection Upstream Splitting Method
BC	Boundary Condition
CFD	Computational Fluid Dynamics
CMC	Ceramic Matrix Composite
C_x	axial chord
DES	Detached Eddy Simulation
DNS	Direct Numerical Simulation
$\bar{e}_2$	area-averaged kinetic energy loss coefficient
FST	Freestream Turbulence
h	span
HPT	High-pressure turbine
k	turbulent kinetic energy
$L_{s,0}, L_{s,1}$	axial location of upstream and downstream measurement stations 0 and 1
LES	Large-Eddy simulation
LPT	Low-pressure turbine
K-H	Kelvin-Helmholtz
Ma	Mach number
P_t	total pressure
(U) RANS	(Unsteady) Reynolds-Averaged Navier-Stokes
Re	Reynolds number
S	Length of loneliness
TKE	turbulence kinetic energy
Ts	turbulent length scale
Tu	turbulence intensity
u, v, w	velocity component
V-K	von Kármán vortex
X, Y, Z	Cartesian coordinate
β	inflow flow angle
ϑ	trailing edge metal angle
γ	specific heat ratio (=1.4)

INTRODUCTION

In the pursuit of enhanced thermal efficiency and increased power output in gas turbines, Ceramic Matrix Composites (CMC) emerge as a pivotal enabling technology due to their lighter weight and elevated thermal limits (approximately 1755 [K]). Employing CMCs as the material for turbine blades challenges the design paradigms originally tailored for metal alloys [1]. Blades crafted from CMC, composed of plies of fabric material, may encounter challenges in adhering to the small radii of curvature typical for metal alloys, necessitating thicker trailing edges.

At the NASA Glenn Transonic Turbine Blade Cascade Facility [2], illustrated in Figure 1, Giel *et al.* undertook a series of experiments to explore the losses of transonic blades featuring varying trailing edge thicknesses (CMC5: 5%, CMC7: 7%, and CMC9: 9% of axial chord). These thicknesses correspond to those achieved by 2 to 4 plies of CMC for the specific blade size under consideration. The experiments covered a broad range of Reynolds numbers ($0.3\times10^6 < Re < 1.9\times10^6$) at low and high free-stream turbulence conditions (turbulence intensity, Tu = 0.5% and 13%), with a constant exit Mach number ($Ma = 0.74$). Depending on Tu and Re, these blades exhibited varying characteristics in profile loss. Giel *et al.* noted a power law scaling dependence of loss on Re, as depicted in Fig. 2. The study reported on one data point that deviated significantly from the power law scaling trend, labeled as an "outlier" and consequently excluded it from the regression process [2]. This "anomaly" is evident in Fig. 2 at $Re = 1.24\times10^6$, where the total pressure loss for CMC9 is shown to experience a sudden increase.

This paper has dual objectives. Firstly, it aims to present the results of a new series of experiments, including a larger sample of Reynolds numbers, conducted to validate that the significant peak in the loss trend of CMC9 at $Re = 1.24\times10^6$ is not merely an experimental artifact and indeed is a 'mound' in the trend. Secondly, the paper seeks to elucidate the mechanism behind this apparent anomaly. Utilizing wall-resolved large eddy simulation (LES) computations, the study demonstrates that the observed phenomenon is attributable to transonic vortex shedding, confirming a hypothesis derived from evidence found in the literature.

SURVEY OF THE LITERATURE

The introduction of a blunt trailing edge on an airfoil carries the potential for instability mechanisms in the wake, including vortex shedding. This phenomenon could markedly amplify blade profile losses and induce unsteady forces on the turbine blade. Cicatelli and Sieverding [3] delved into the unsteady behavior of a turbine blade wake by drawing parallels with flow behind a cylinder. Pioneering works on vortex shedding by Gerrard [4] and Lienhard [5] contributed to the further understanding of vortex shedding, highlighting distinct shedding patterns: periodic vortex shedding, *i.e.*, von Kármán (V-K) vortices for low Reynolds numbers ($Re < 150$), a transition to turbulent wake for $150 < Re < 300{,}000$, and turbulent vortex sheet for $Re > 300{,}000$.

The complexity of vortex shedding behind a cylinder increases under transonic conditions, primarily due to interactions with pressure waves. Frequencies associated with shed vortices' oscillations become coupled with the pressure waves, as observed by Hoffmann [6]. Insights from these well-established observations of wake patterns behind a cylinder are central to the understanding of turbine blade wake behavior, especially in transonic conditions and characterized by high Reynolds numbers.

In the transonic regime, the von Kármán vortex street persists but as one among various transient vortex shedding patterns. Carscallen *et al.* [7] investigated the Eckert-Weise effect, revealing that vortex cores in the wake have lower temperatures, impacting losses in the transonic regime, including a thermo-acoustic effect where the vortex cores have colder temperatures than the surrounding fluid. This effect is associated with hot spots at the edge of the wake. Sieverding *et al.* [8] conducted experiments on a transonic VKI blade, confirming the significant impact of vortex shedding on steady and unsteady pressure and temperature distributions in the wake. El-Gendi [9] *et al.* performed a Detached Eddy Simulation (DES), highlighting temperature variations. Vagnoli *et al.* [10] used LES to study the interaction between vortex shedding and oblique shocks, emphasizing the role of an unstable vortex street in influencing trailing edge pressure fields and overall losses.

Wang *et al.* [11] demonstrated through DES the sensitivity of wake vortex street formation to slight changes in suction side curvature. Leonard *et al.* [12] conducted a grid sensitivity analysis for RANS, Unsteady RANS (URANS), and LES, emphasizing the importance of highly resolved LES for accurate predictions in the transonic regime.

Despite advancements in High-Performance Computing, computational time for LES (and Direct Numerical Simulation (DNS)) remains non-trivial, particularly for high-Re applications. Studies by Chapman [13], Choi and Moin [14], Tyacke *et al.* [15], and Ameri [16] provide insights into grid requirements for simulating turbines with LES.

Several studies have employed wall-modeled/resolved LES to model aerodynamics of transonic low- and high-pressure turbine blades. Papadogiannis [17] performed a wall-modeled LES using the engine-representative MT1 transonic high-pressure turbine (HPT) blade using a mesh count of 114 million. It is shown that improving near wall grid resolution coupled with a near-wall model has an impact on the increase of the level of turbulent structures, boundary layer thickness as well as near-

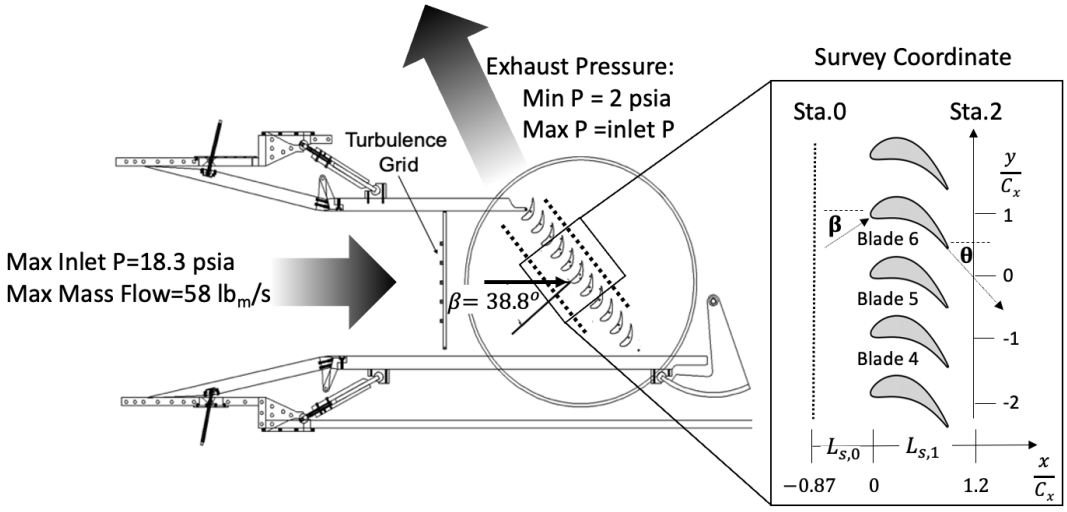

FIGURE 1: OVERVIEW OF THE EXPERIMENTAL FACILITY AT NASA GLENN RESEARCH CENTER

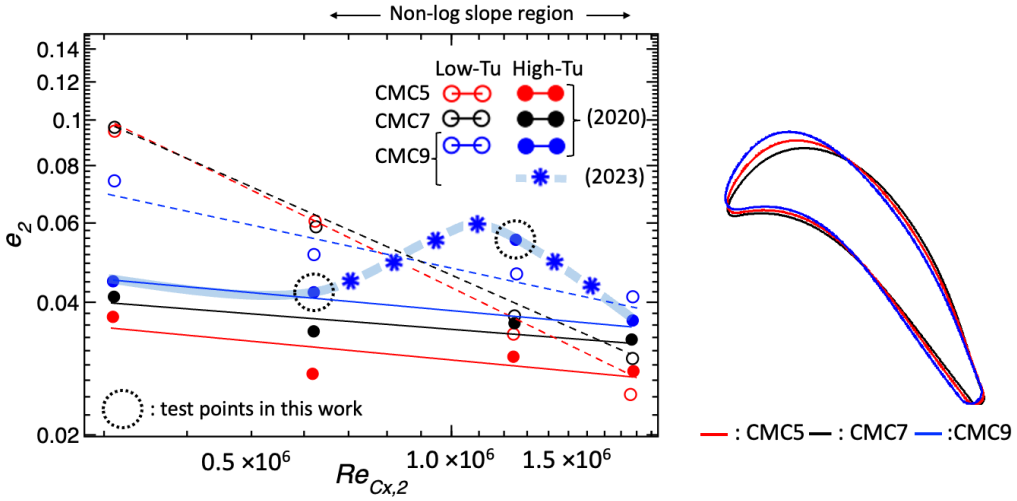

FIGURE 2: EXPERIMENTAL RESULTS OF THE AREA-AVERAGED KINTIC ENEGY COFFECIENTS (CIRCLE: 2020 AND STAR: 2023). THE DASHED LINES ARE DATA FITS BASED ON LOG_SCALE.

wall dynamics. Zhao and Sandberg [18] performed a highly resolved LES to model the LS89 HPT vane for the high-*Ma* number range ($0.7 < Ma < 1.1$ and $520{,}000 < Re < 580{,}000$) using 630-1450 million elements. Coupled with entropy loss analysis, they decomposed the overall loss into different source terms and were able to identify the regions where the loss is mainly generated. Recently, with the help of GPU-accelerated computations, the same research group demonstrated capturing the effect of micron-scale surface roughness on the transonic flow around the LS89 HPT vane using DNS (the mesh count is 7.3 billion elements) [19]. It is demonstrated there that roughness shifts the boundary layer transition on the suction side further upstream, producing more turbulent kinetic energy and larger wake losses. Finally, Rossiter *et al.* [20] found an intriguing phenomenon, so-called "transonic vortex shedding," (also see [21]) using the wall-resolved LES to model the flow field around a single, symmetrical plate mounted between two interchangeable liners under transonic conditions. The loss increased at the specific Reynolds number at the same exit Mach number. The detached vortex shedding occurs for $Re < 600{,}000$, and the transonic vortex shedding associated with 100% increase in the loss takes place for $Re > 900{,}000$. The wall-resolved LES with 200 million elements accurately captures this unique trend of the loss profile against *Re* and the effect of the trailing edge wedge angle.

EXPERIMENTAL SETUP AND RESULT

Details of the experimental configurations and methods were presented by Giel *et al.* [2] but will be summarized here.

Blade loading and total pressure wake loss measurements were acquired in NASA's Transonic Turbine Blade Cascade using ten blades, the center three of which were instrumented with static pressure taps. The separate air supply and vacuum exhaust systems allow for independent control of the exit Reynolds number and exit Mach number. An upstream turbulence grid was used for some cases to generate engine-realistic turbulence levels of $Tu \approx 13\%$. Without the grid, $Tu \approx 0.5\%$. A pneumatic five-hole probe was traversed at $x/C_x \approx 1.20$ across three blade pitches to determine the wake total pressure loss profiles. Three blade sets were examined with varying trailing edge thickness of 5%, 7%, and 9% of axial chord, designated as CMC5, CMC7, and CMC9, respectively. The wake profiles were integrated to determine a kinetic energy loss coefficient, $\bar{e}_2$, as defined in [2]. The variation of $\bar{e}_2$ with Re was found to follow a power law correlation quite closely for all cases except one. For CMC9 at high inlet Tu, the loss coefficient at $Re = 1.24\times10^6$ was anomalously high but came back down to the power law correlation level for $Re = 1.86\times10^6$ as shown in Fig. 2. Subsequent to the original measurements, the facility data acquisition system was updated, and this case was used as a validation case. The repeated Re points matched very well, so intermediate Re points were acquired to help explain the anomaly. The six new data points are shown with star symbols in Fig. 2 and indicate a clear physical trend that was suspected to result from transonic vortex shedding.

TABLE 1: TEST CONDITION

	Low-Re	High- Re
P_1 [psia]	5.003	10.102
$P_{t,1}/P_2$	1.44	1.44
Re_2	621,900	1,246,350
Ma_2	0.741	0.740
Tu_{in} [%]	13	13
Ts/C_x	0.02	0.02
β [deg.]	38.8	38.8

NUMERICAL SETUP

In this investigation, we employed the in-house code, Glenn-HT [22], a tool developed at NASA Glenn Research Center for solving the unsteady compressible Navier-Stokes equations. Glenn-HT utilizes structured multi-block grids and a dual time-stepping procedure, implicitly advancing the solution in physical time. Achieving second-order temporal accuracy, an explicit four-stage Runge-Kutta scheme is employed. The AUSM+-up scheme [23], coupled with the 2nd order limiter of the MUSCL scheme, is used for evaluating inviscid fluxes.

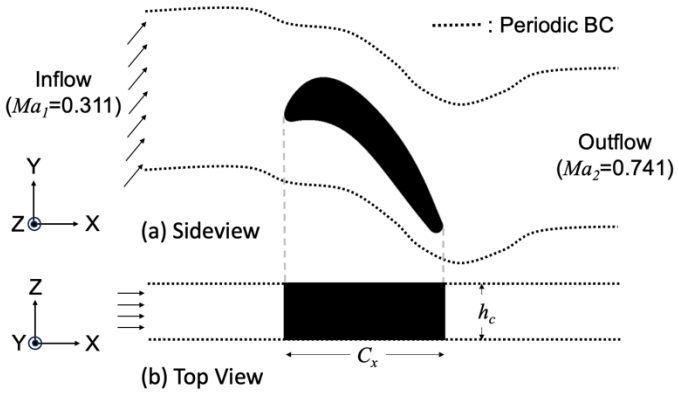

FIGURE 3: COMPUTATIONAL DOMAIN

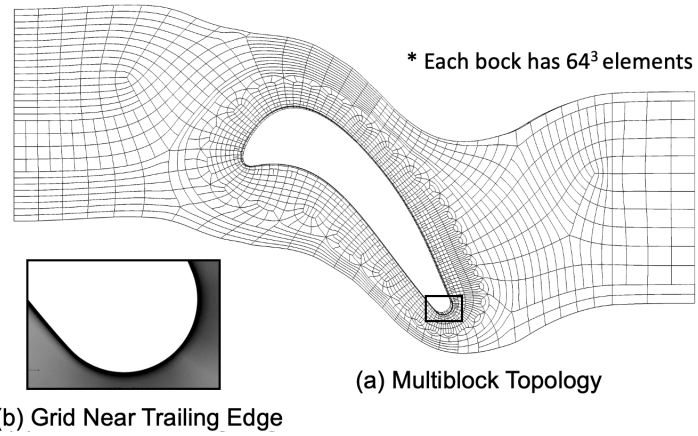

FIGURE 4: GRID AND MULTIBLOCK TOPOLOGY

Concerning turbulence modeling, a large eddy simulation with the localized dynamic k-equation model (LDKM) proposed by Kim and Menon [24] is utilized. LDKM dynamically evaluates model coefficients in the Reynolds stress and the dissipation rate based on the assumption [25] that "similarity" exists in the nature of isotropic turbulence between the largest unresolved scales and the smallest resolved scales. The detailed explanation of LDKM may be found in [24]. The LDKM model implemented in the Glenn-HT code has been successfully applied to turbomachinery applications (see [26]-[28]).

Boundary Conditions and the Mesh

The flow conditions for the current numerical simulations are summarized in Table 1, and the computational domain schematic is shown in Fig. 3. While the inlet endwall boundary layer thickness is significant, we focused on the midspan section of the domain ($\Delta h/C_x = 0.1$). Periodic boundaries are imposed in the spanwise direction (dash-dot-

line). For the inlet boundary, *Tu* and turbulence integral length scale (*Ts*) are specified based on experimental conditions [29]. Note that the turbulence grid did not align against the blade row (see Fig. 1), resulting in a pitchwise variation in *Tu* measured at Station 0 [29]. The inlet turbulence intensity was 13%, and pitchwise variance was ± 2.6% over the center passage.

For inflow turbulence, the digital filtering approach developed by Klein *et al.* [30] is employed. It is confirmed that u'_{rms}/U_0, v'_{rms}/U_0, and w'_{rms}/U_0 constitute isotropic incoming turbulence, and cross-components ($u'v'$, $u'w'$, and $v'w'$) are almost zero [29]. The spectral slope follows the Kolmogorov –5/3 law in the upstream region of the blade.

The mesh requirement for wall-resolved LES at such high-Re application (*Re*~*1,246,350*) is significant. Using the scaling rule proposed by Chapman [13] (also Choi and Moin [14]), the mesh resolution was scaled up to 175 million elements from the 50 million mesh, which we used for *Re*~621,900 (In [29]), we have examined the effect of the grid resolution in detailed.) This grid resolution is indeed comparable to the one used by [20] (200 million elements used for 300,000 < *Re* < 2500,000). In this study, we refined the mesh further, especially near the trailing edge, ensuring y_1^+ is close to unity over the blade. There are about 1,000 points in the circumferential direction at the trailing edge. The resulting mesh count is 290 million elements. Considering Rossiter et al. used a span of $0.04\times C_x$ for a relevant test condition, we set the span of the domain to $0.1\times C_x$. A spanwise grid resolutions of 64 points was employed in the present computations. In the midspan wall region, on average, x_1^+ value is ~10, and z_1^+ is ~20. The multiblock topology and grid resolution near the trailing edge are shown in Fig. 4.

RESULTS

We used 2,000 processors (Xeon Gold 624877) on Pleiades at NASA Advanced Supercomputing facilities, and the computational times are 1 million CPUs.

Figures 5 (a)–(c) show the calculated pressure coefficients along the blade surface, the wake profiles at the midspan and the area-averaged kinetic energy loss coefficients, $\bar{e}_2$:

$$\bar{e_2} = \frac{\left(\frac{P_{t,1}}{\overline{P_{t,2}}}\right)^{\frac{\gamma-1}{\gamma}} - 1}{\left(\frac{P_{t,1}}{P_2}\right)^{\frac{\gamma-1}{\gamma}} - 1}$$

where $P_{t,1}$ and $\overline{P_{t,2}}$ are the total pressure at the inlet and the exit, and P_2 is the static pressure at the exit. γ is the specific heat ratio

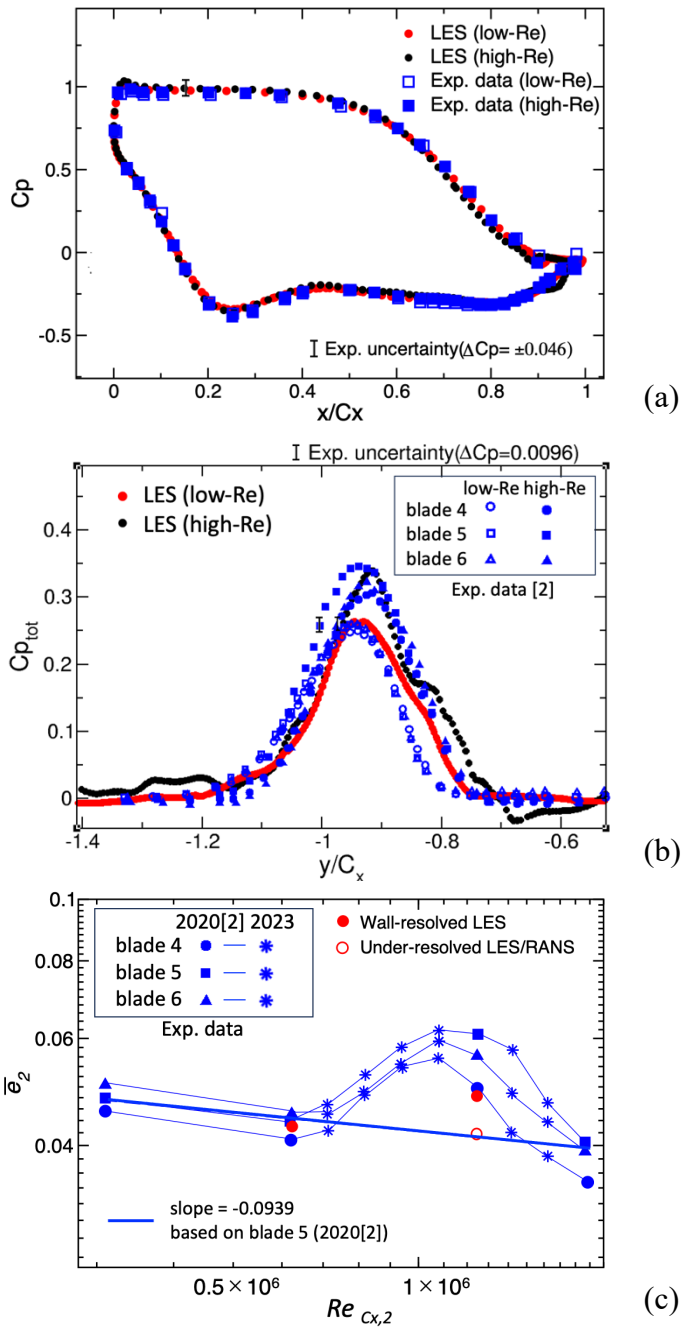

FIGURE 5: (a) PRESSURE COEFFICENTS, (b) WAKE PROFILE, AND (c) AREA-AVERAGED KINETIC ENRGY COEFFICIENTS.

(=1.4). For the pressure coefficient, reasonable agreement is achieved for both low- and high-*Re* cases. The experimental data shows a slightly lower pressure coefficient near the trailing edge at the high-*Re* condition, which LES is able to capture. However, there is a small discrepancy in the upstream region of the suction side where LES seems to predict a more separated flow. We will discuss this in more detail later. For the wake prediction, although the agreement between the prediction and the experimental data is not excellent for the high-*Re*, LES indeed is

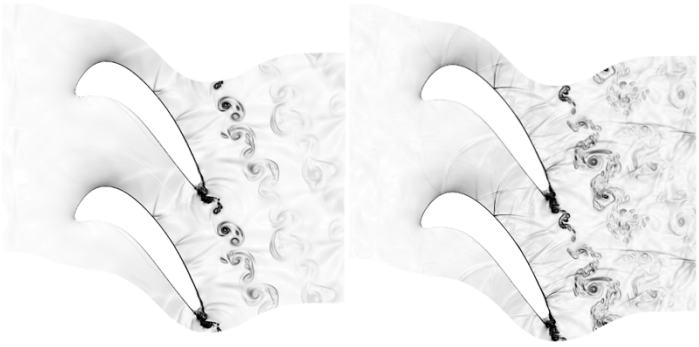

FIGURE 6: NUMERICAL SCHLIEREN FOR (a) LOW-RE AND (b) HIGH-RE FLOWS.

able to predict the higher loss for the high-*Re* number case. Under-resolved LES and RANS were not capable of capturing this kind of a higher loss at the high-*Re*. The predicted losses were about 0.04, which follow the log-scale-based interpolation (dashed line). The resulting area-averaged kinetic energy loss coefficients at low- and high-*Re* number conditions are 0.42 and 0.49, respectively. Although the experimental data shows a higher value (0.55±0.05) than our prediction at the high-*Re*, this result is encouraging, and this motivated us to perform further analysis of this phenomena.

Figure 6 show the instantaneous numerical schlieren for (a) the low-*Re* and (b) high-*Re* using the wall-resolved LES. Although both cases show the vortex shedding (*i.e.,* von Kármán vortices) near the trailing edge, there are notable differences in the characteristics of the flow fields. First, in the high-*Re*, the V-K vortices are coupled with the small vortices, and the edges of each vortex are discontinuous. Also, these vortices persist well downstream, indicating that there is strong turbulent motion generated near the trailing edge. Second, there is a train of pressure waves traveling within the computational domain, particularly on the suction side and in the wake. These pressure waves seem to be generated from the wake perturbation and the large structure of vortices in the downstream regions. The distinct "V" shape of the waves on the suction side indicates the strong reflected waves formed on the wall. For the low-*Re*, the shape (and edge) of each V-K vortex looks more organized, and there is less turbulent motion. In addition, the pressure waves are weaker. In fact, these pressure waves do not interact with the vortices much in the downstream region. Compared with the numerical schlieren shown by Rossiter et al., (see Fig. 1 in [20]), we found great similarity between our prediction and theirs in the sense that there are pressure waves around the blade. However, in our case, there is no turbulent boundary layer on the pressure side (there is no boundary layer trip in our calculation), and the strength of the pressure waves seem to be weaker in our results. Also, in [20], there is not much interaction between the pressure waves and the vortices downstream, which is clearly seen in our result. Figures 7 (a) and (b) depict the three-dimensional instantaneous structure of vortices near the trailing edge for the low- and high-*Re* cases. For the high-*Re*, it is observed that there is very active motion of the boundary layer on the suction surface, which starts just at the foot of the strong pressure wave. This may indicate transition from laminar to turbulent flow, separation, or significant perturbations of the boundary layer (from this figure, it is not clear which one is the root-cause). Please note that since the turbulent boundary layer is generated by the trips in [20], these pressure waves do not initiate transition and separation in their calculation). In addition, it is not clear whether this pressure wave is generated as a result of a sudden change of boundary layer thickness due to transition/separation or is due to the wake perturbation (*i.e.,* vortex shedding). In the downstream region, very large V-K

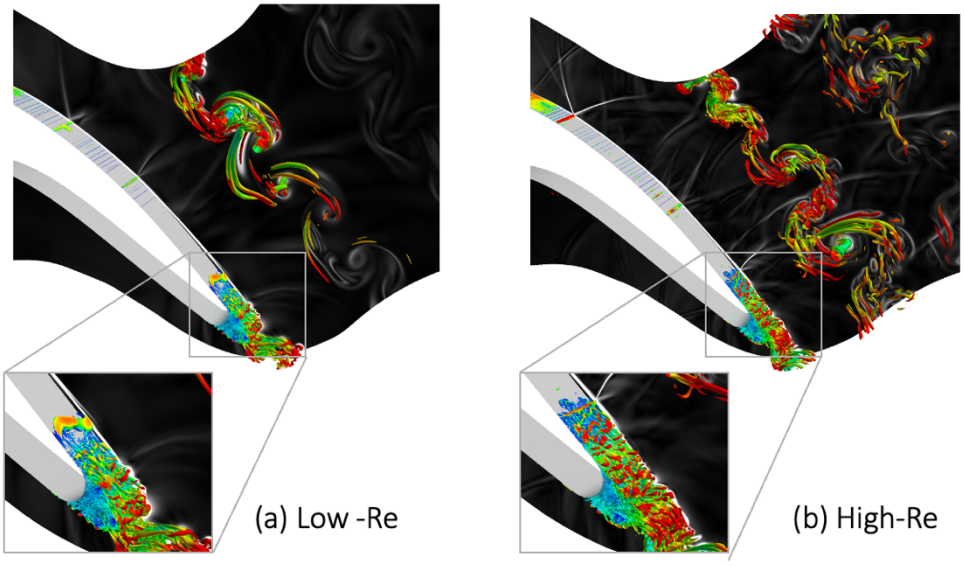

FIGURE 7: ISO-SURFACE OF Q-CRITERION COLORED BY NORMALIZED TOTAL PRESSURE (BLUE:0.5, RED:1.0) AMD CONTOUR OF PRESSURE GRADIENTS (BACK:0, WHITE:1)

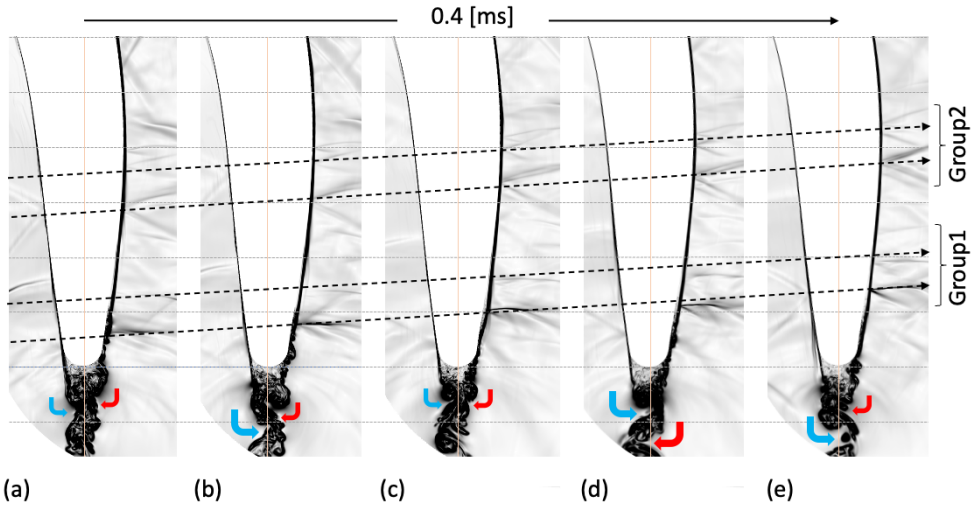

FIGURE 8: NUMERICAL SCHLIERENS AT FIVE DIFFERENT TIME INSTANCES

vortices are developed and coupled with small secondary vortices. For the low-*Re*, the transition seems to occur without any interaction with the pressure wave. For both cases, there are small recirculation bubbles on the upstream of the suction side, and these recirculation bubbles are due to "intermittency". This intermittent motion can perturb the boundary layer as well.

To investigate the unsteadiness of the pressure wave located at the transition point in Fig. 7, we examine the numerical schlieren at a sequence of five time instances (see Fig 7). There

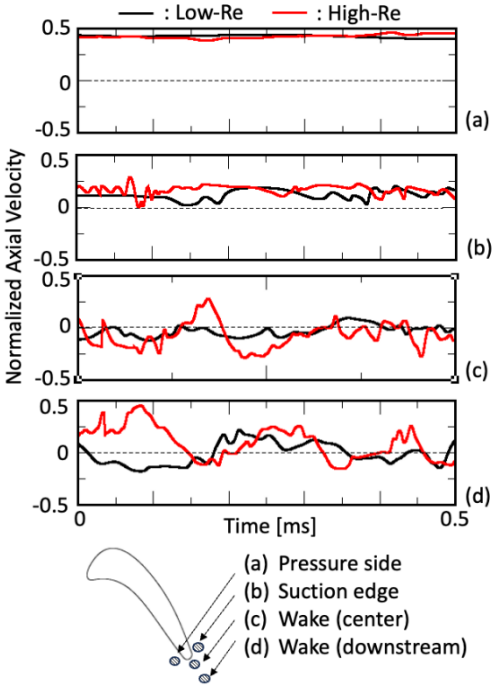

FIGURE 9: HISTORIES OF NORMALIZED AXIAL VELOCITY

are two groups of pressure waves, and each of them includes two pressure waves. These groups are traveling upstream at the same speed. Compared with the strength of the pressure waves on the suction sides, the ones on the pressure side are much weaker. Also, during 0.4 milliseconds, the pressure side vortex (see blue arrows) appears to be stronger than suction side vortex. This observation is consistent with the work done by Han and Cox [31]. It seems that the pressure waves significantly perturb the boundary layer on the suction side while traveling upstream. Finally, there are several frequencies involved in the oscillations of vortices shedding in addition to those associated with the V-K instability (this is evidenced by the synchronized vortex shedding seen in Fig. 7 (c)).

In Figure 9, the histories of normalized axial velocity are shown for four locations: (a) at the edge of pressure side, (b) at the edge of suction side, (c) at the center of wake, and (d) downstream of the wake. Near the pressure side, both the low-*Re* (black) and high-*Re* (red) show relatively constant velocities. Near the suction edge, there is much more intermittent motion observed at high-*Re* (see Fig. 9 (b)). In the wake region, the high-*Re* case shows much stronger motion, and a periodic motion can also be observed in Fig. 9 (d). Compared with Fig. 8, it follows that each vortex shedding event does not generate a strong pressure wave.

Figure 10 shows the contours of axial velocity near the suction surface at three different time instances (Fig. 10 (1a)-(1c)) and the time-averaged solution (Fig.10 (2)) and the contours of the magnitude of the density gradient. There are several key findings to be addressed.

There are roughly four categories of flow features observed: (a) local recirculation bubble, (b) large recirculation bubble/separation, (c) strongly disturbed flow region, and (d) transition to turbulent boundary layer. The small recirculation

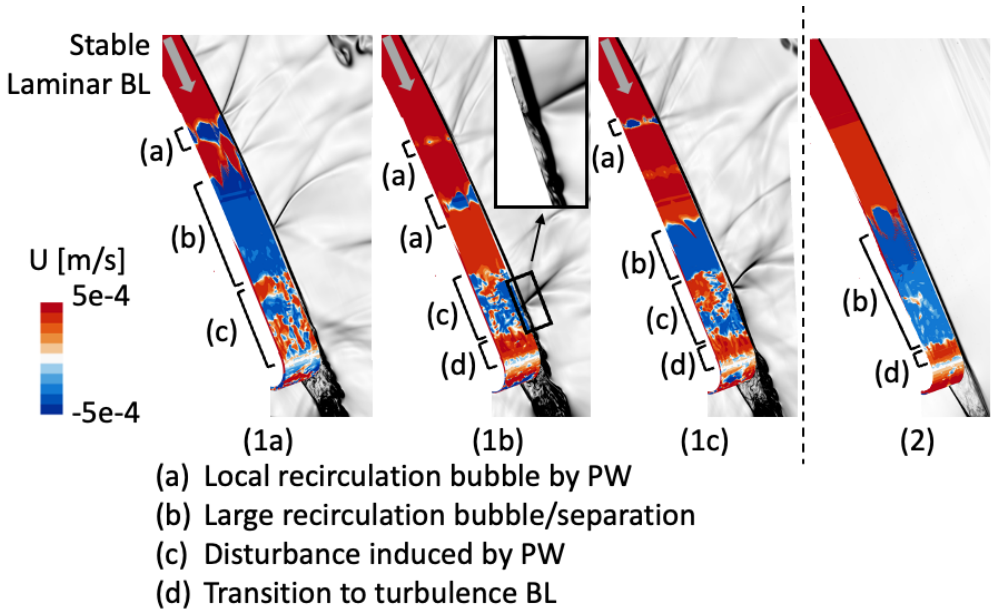

FIGURE 10: (1a-1c) CONTOURS OF INSTANTANEOUS NORMALIZED AXIAL VELOCITY NEAR THE SUCTION SURFACE AND (2) THE TIME-AVERAGED PROFILE

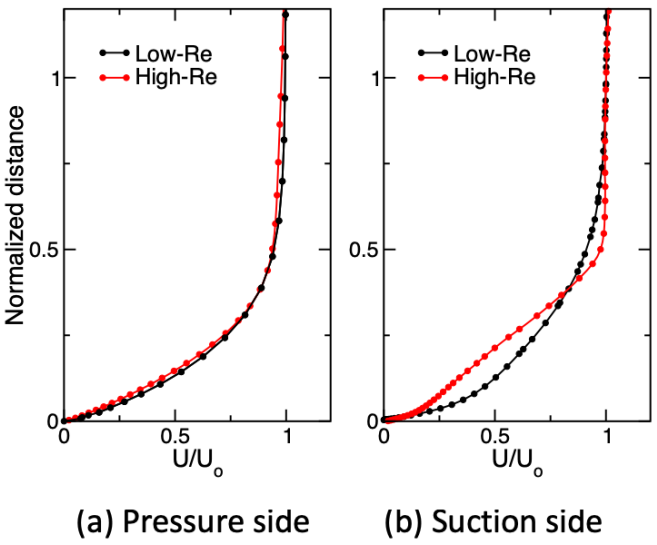

FIGURE 11: NORMALIZED AXIAL VELOCITY PROFILES AT THE EDGE OF (a) PRESSURE SIDE AND (b) SUCTION SIDE

regions typically observed upstream are caused by the passing of the pressure waves or intermittency, and the flow is quickly reattached. There are instances where a substantial recirculation region forms downstream (refer to Fig. 10 (1a) and (1c)). However, it is important to note that this large recirculation bubble is not consistently present. In the vicinity of the trailing edge, the flow field experiences significant disruptions due to the influence of the pressure waves, followed by a transition region. Remarkably, this disturbance persists for some time even after the pressure wave has propagated away from the region.

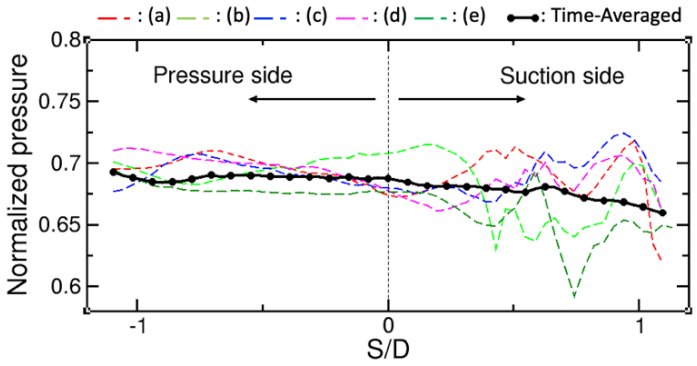

FIGURE 12: NORMALIZED PRESSURE ON THE TRAILING EDGE SURFACE. FOR SYMBOLS, SEE FIG 8.

The key inference drawn from these findings is that the boundary layer on the suction side exhibits a high level of unsteadiness. Furthermore, the locations of recirculation, transition, and reattachment are notably affected by the traveling pressure waves.

Figures 11 (a) and (b) present a comparison of the normalized axial velocity profiles at the edges of the pressure side and the suction side for both low-*Re* (depicted in black) and high-*Re* conditions. On the pressure side, both scenarios exhibit very similar profiles. However, on the suction side, a fuller profile is observed for low-*Re,* contrasting with the less pronounced profile for high-*Re*. Our prior research [29] indicates that a turbulent boundary layer forms at the edge of the suction (i.e., immediately upstream of trailing edge) side after bypass transition. As illustrated in Fig. 10, pressure waves induce a highly unsteady flow on the suction side for the high-*Re* case.

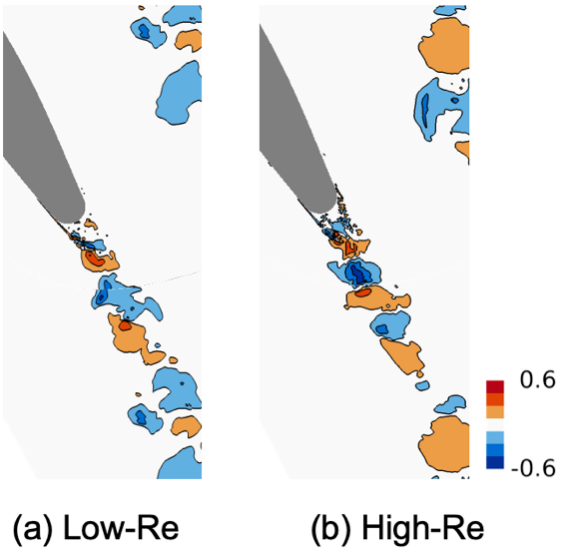

FIGURE 13: NORMALIZED AXIAL VELOCITY FLUCTUATIONS

Consequently, the resulting velocity profile does not appear as full. This could be responsible for the wider suction side wake shown in [2].

Given the highly unstable wake and boundary layer on the suction side, we assess whether the assumption of an isobaric condition in the wake region holds true. For this purpose, Fig. 12 displays the instantaneous trailing edge base pressure profiles at five different time instants (labeled (a) to (e) in Fig. 8) and the time-averaged profile. The analysis reveals that the pressure profiles remain relatively constant on the pressure side but exhibit high instability on the suction side. This instability arises due to the presence of numerous eddies traveling from the center of the wake to the edge of the suction side (see Fig. 8 (d)). Although there is a 5% decrease in the pressure from the pressure side to the suction side, the time-averaged profile appears relatively flat (*i.e.,* the isobaric condition is most likely held in this case.)

To investigate the strength of the V-K vortices, the normalized axial velocity fluctuation ($= (u - \bar{u})/u_o$) is calculated for the low-*Re* and the high-*Re* (see Fig.13). Here, $\bar{u}$ and u_o are the time-averaged axial velocity and the reference velocity ($=\sqrt{RT}$). Although both cases show the periodic pattern of velocity fluctuation, high-*Re* shows a much more intense and chaotic velocity field in particular near the wake (i.e., strong swinging motion of the wake). Also, there are more active motion near the edge of the suction side. Another important factor of vortex shedding is the energy separation effect [7] (*i.e.,* the Eckert–Weise effect). This thermo-acoustic effect is critical for the transonic regime in terms of the losses. To this end, the normalized temperature fluctuation ($= (t - \bar{t})/t_{1,t}$) is calculated. For both cases, there are hot spots at the edge of the shear layer (and the wake) and cold spots at the vortex cores. For

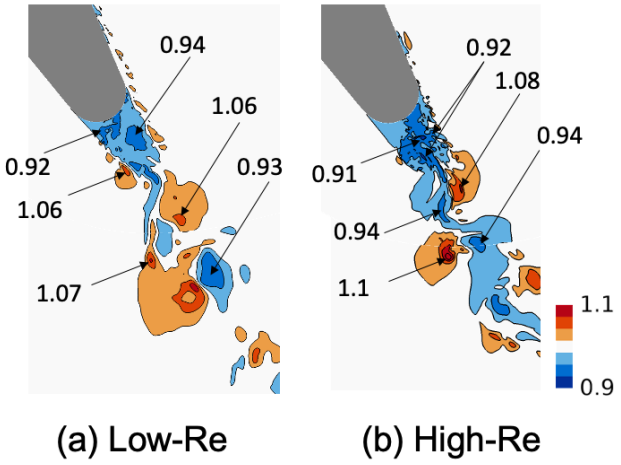

FIGURE 14: NORMALIZED TEMPERATURE FLUCTUATIONS

the high-*Re* (see Fig. 14 (b)), the temperatures of hot and cold spots are ~10% higher and lower than inlet total temperature. The energy separation effect is more pronounced for the high-*Re*. Also, there are a variety of small size cold spots associated with the vortex cores near the edge of the suction side. This is consistent with the observation of Fig. 12.

From these results, we may conclude that there is more unstable and stronger vortex shedding in the wake for the high-*Re*, which can lead to a bigger loss.

Perturbation of the Pressure Waves

In this subsection, our objective is to conduct a perturbation analysis to gain insights into the attenuation or persistence of pressure wave perturbations under two specific conditions under investigation. To achieve this, we introduce perturbations to the velocity field within the red box (refer to Fig. 15), resulting in the generation of robust pressure waves on both the pressure and suction sides.

In the case of low Reynolds number (low-*Re*), the induced pressure waves rapidly diminish, with no significant waves present within 0.4 milliseconds. The resulting flow field closely resembles the scenario without perturbations. Conversely, under high Reynolds number (high-*Re*) conditions, the induced strong pressure waves persist on both sides for 0.4 milliseconds, with only the suction side retaining strong pressure waves after 1.0 millisecond. Despite this, the resulting flow field resembles that without perturbations.

This analysis highlights a crucial observation: there exists a mechanism that consistently generates pressure waves exclusively on the suction side, particularly under high-*Re* conditions.

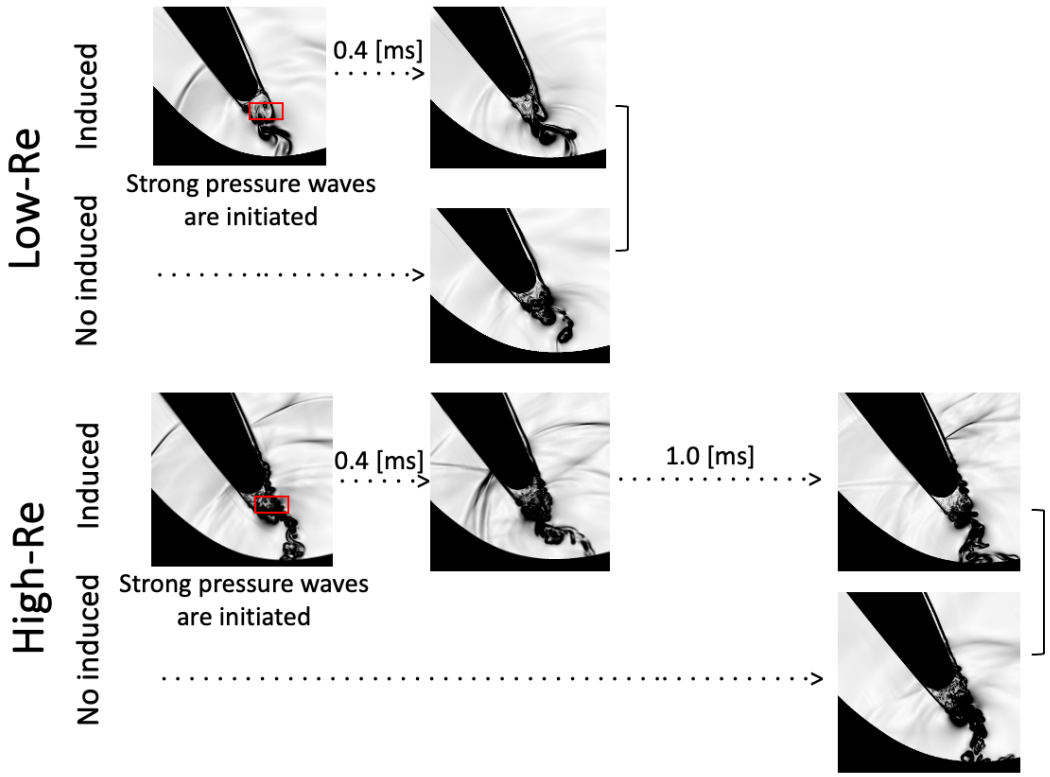

FIGURE 15: (top) LOW-RE PRESSURE WAVES WITH/WITHOUT PERTURBATION AND (bottom) HIGH-RE PRESSURE WAVES WITH/WITHOUT PERTURBATION.

Discussion

Through the analysis presented in this paper, we have uncovered compelling evidence indicating that a high Reynolds number is associated with a more pronounced pressure wave coupled with an unstable wake resulting from von Kármán vortex shedding. This mechanism is illustrated schematically in Fig. 16. In contrast to the work conducted by Rossiter, Pullan, and Melzer in 2022, the turbulent boundary layer is naturally introduced to the wake through flow separation and transition processes, denoted by (c). The locations of separation and transition are significantly influenced by pressure waves traveling along the suction side, indicated by (b1). Furthermore, the pressure wave is potent enough to substantially perturb the boundary layer, enhancing the unsteadiness of vortex shedding, as noted by (a), which, in turn, generates subsequent pressure waves.

Moreover, the size of the eddies in the downstream region (i.e., the von Kármán vortex street (b2)) is substantial enough to produce pressure waves. Ultimately, the intermittency or residual effect of the pressure wave can generate a local recirculation bubble (see (e) and (d) in Fig.16), providing another source of boundary layer perturbation, namely skin vortices [11]. It seems that there exists a delicate balance among these mechanisms to sustain this feedback system. By keeping this balance in mind, a better understanding of the experimental data (see Fig. 2) might be achievable. Two key questions arise: "Why does CMC9 exhibit a distinct anomaly in the loss?" and "What is the cause of the local peak in the loss?"

The first question can be addressed in terms of disturbance production. Compared with blades with smaller trailing edge thickness (e.g., CMC5 and CMC7), CMC9 is likely to experience more perturbations due to the larger size of the wake under the same operating conditions. Various sizes of eddies formed in a large wake are coupled with vortex shedding at the shear layer. Addressing the second question is less straightforward. For low-*Re* conditions, the flow has less inertia given an exit Mach number and the same blade shape. Consequently, the strength of compression is weaker than that in high-*Re* flows when the flow is blocked similarly. Thus, the source of pressure wave generation is diminished. In the experiments, losses become significantly smaller at much higher *Re* (approximately 2×10^6). This phenomenon may be explained by the increased force required to block the flow with greater inertia, resulting in the generation of compression waves given the same exit Mach number. When the Reynolds number becomes sufficiently high, these strong forces may no longer be available, potentially explaining the local peak observed in the experimental data.

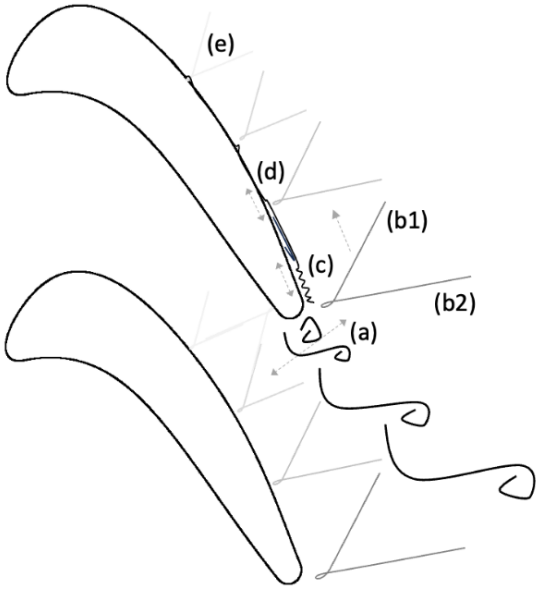

FIGURE 16: SCHEMATIC OF FEEDBACK SYSTEM OF UNSTABLE WAKE COUPLED WITH PRESSURE WAVES

To generate the required strong forces (*i.e.,* perturbations) for pressure wave generation under high-*Re* conditions, an additional mechanism may be necessary. For example, Rossiter *et al.* employed a "trip" to induce a turbulent boundary layer on both pressure and suction sides, as described in their 2022 work, achieving transonic vortex shedding and high losses even at very high *Re* (2,500,000).

CONCLUSIONS

In this paper, we conducted a series of new experiments to validate that the "anomaly" observed in the loss profile of CMC9 in previous campaigns [2] is not merely an experimental artifact. The newly acquired data reveals a gradual increase in losses starting at *Re*=700,000, reaching a local maximum at 1,100,000, and then decreasing thereafter. To comprehend this phenomenon, we carried out wall-resolved large eddy simulations at two specific test points: *Re*=621,900 and 1,246,350.

Our numerical results indicate that the high-*Re* case exhibits a significantly perturbed wake due to the presence of pressure waves traveling along the suction side, disrupting the boundary layer. The locations of separation, reattachment, and transition are highly unsteady. In contrast, for the low-*Re* case, the pressure waves are much weaker, and the feedback system between the unstable wake and the generation of pressure waves is not sustained. This study establishes that there exists a specific Reynolds number range under which strong pressure waves are coupled with an unstable wake and boundary layer through von Kármán vortex shedding. This phenomenon bears similarities to transonic vortex shedding. However, the presence of the supersonic flow region is localized, and the strength of the pressure waves is comparatively weak. Consequently, the increase in losses is moderate.

ACKNOWLEDGEMENTS

This work was supported by Dr. Laura Evans for the NASA Hybrid Thermally Efficient Core project. The authors would like to acknowledge their insightful discussions on transonic vortex shedding with Dr. Thomas Praisner. The authors also would like to thank Mr. Timothy Beach, Dr. David Rigby, Dr. Paht Juangphanich and Dr. Erlendur Steinthorsson for their assistance in preparing and running the simulations. The simulations were conducted on the NASA Advanced Supercomputing (NAS) Pleiades computer cluster.

. REFERENCES

[1] Boyle, R. J., Gnanaselvam, P., Parikh, A. H., Ameri, A. A., Bons, J. P., and Nagpal, V. K. 2021. "Design of Stress Constrained SiC/SiC Ceramic Matrix Composite Turbine Blades." ASME Journal of Engineering for Gas Turbine and Power: 143(5): 051013.

[2] Giel, P., Shyam, V., Juangphanich, P., and Clark, J. P., 2020, “Effects of Trailing Edge Thickness and Blade Loading Distribution on the Aerodynamic Performance of Simulated CMC Turbine Blades”, Proceedings of the ASME Turbo Expo, Virtual, GT2020-15802.

[3] Cicatelli, G., and Sieverding, C.H., 1996, “A Review of the Research on Unsteady Turbine Blade Wake Characteristics. In Loss Mechanisms and Unsteady Flows in Turbomachinery”, AGARD CP 571; AGARD: Neuilly-Sur-Seine, France, 1996.

[4] Gerrard, J. H., 1966, “The Mechanics of the Formation Region of Vortices Behind Bluff Bodies”. Journal of Fluid Mechanics: 25, pp. 401–413.

[5] Lienhard, J. H., 1966, "Synopsis of Lift, Drag and Vortex Frequency Data for Rigid Circular Cylinders", Technical Extension Service, Bulletin 300, College Engineering, Washington State University.

[6] Hoffmann, J., and Weiss, D. A., 2023, “Compressible and Viscous Effects in Transonic Planar Flow around a Circular Cylinder—A Numerical Analysis Based on a Commercially Available CFD Tool”, Fluids; 2023, 8, 182.

[7] Carscallen, W. E., Fleige, H. U., and Gostelow, J. P., 1996, “Transonic Turbine Vane Wake Flows”, In: Turbomachinery, 1996, pp. V001T01A109.

[8] Sieverding, C. H., Ottolia, D., Bagnera, C., Comadoro, A., Brouckaert, J.-F., and Desse, J.-M., 2004, “Unsteady Turbine Blade Wake Characteristics”, ASME Journal of Turbomachinery: 126, pp. 551–559.

[9] El-Gendi, M. M., Ibrahim, M. K., Mori, K., and Nakamura, Y., 2010, “Energy Separation in High Subsonic Turbine Cascade”. Transactions of the Japan Society for Aeronautical and Space Sciences: 52, pp. 206–212.

[10] Vagnoli, S., Verstraete, T., Mateos, B., Sieverding, C., 2015, “Prediction of the Unsteady Turbine Trailing Edge Wake Flow Characteristics and Comparison with Experimental Data”, Proceedings of the Institution of Mechanical Engineers, Part A, Journal of Power and Energy: 229 (5), pp. 487-497.

[11] Wang, S., Wen, F., Zhang, S., Zhang, S., and Zhou, X., 2018, “Influence of Trailing Boundary Layer Velocity Profiles on Wake Vortex Formation in a High Subsonic Turbine Cascade”. Proc. IMechE Part A J. Power Energy: 233, pp. 186–198.

[12] Leonard, T., Gicquel, L. Y. M., Gourdain, N., and Duchaine, F., 2015, “Steady/unsteady Reynolds Averaged Navier-Stokes and Large Eddy Simulation of a Turbine Blade at High Subsonic Outlet Mach Number”, ASME Journal of Turbomachinery: 13: (4): 041001.

[13] Chapman, D., 1979. “Computational Aerodynamics Development and Outlook”. AIAA Journal: 17(12), pp. 1293–1313.

[14] Choi, H., and Moin, P., 2012, “Grid-Point Requirements for Large Eddy Simulation: Chapman’s Estimates Revisited,” Physics of Fluids: 24, p. 011702.

[15] Tyacke, J., Vadlamani, N. R., Trojak, W., Watson, R., Ma, Y., and Tucker, P. G., 2019, “Turbomachinery Simulation Challenges and the Future,” Prog. Aerosp. Sci., 110, pp. 10054.

[16] Ameri, A., 2016, “Requirements for Large Eddy Simulation Computations of Variable-Speed Power Turbine Flows,” Technical Report, NASA/CR, 2016-218962.

[17] Papadogiannis, D., Duchaine, F., Sicot, F., Gicquel, L., Wang, G., and Moreau, S., 2014, “Large Eddy Simulation of a High Pressure Turbine Stage: Effects on Sub-Grid Scale Modeling and Mesh Resolution”. Proceedings of the ASME Turbo Expo 2014 Gas Turbine Technical Congress and Exposition, no. Paper No. GT 2014-25876.

[18] Zhao, Y., and Sandberg, R. D., 2021, "High-Fidelity Simulations of a High-Pressure Turbine Vane Subject to Large Disturbances: Effect of Exit Mach Number on Losses", ASME Journal of Turbomachinery: 143(9): 091002.

[19] Nardini, M., Jelly, T. O., Kozul, M., Sandberg, R. D., Vitt, P., and Sluyter, G., 2023, "Direct Numerical Simulation of Transitional and Turbulent Flows Over Multi-Scale Surface Roughness—Part II: The Effect of Roughness on the Performance of a High-Pressure Turbine Blade." ASME Journal of Turbomachinery: 146(3): 031009.

[20] Rossiter, A. D., Pullan, G., and Melzer, A. P., 2023, "The Influence of Boundary Layer State and Trailing Edge Wedge Angle on the Aerodynamic Performance of Transonic Turbine Blades." ASME Journal of Turbomachinery: 145(4): 041008.

[21] Melzer, A. P., and Pullan, G., 2019. “The Role of Vortex Shedding in the Trailing Edge Loss of Transonic Turbine Blades”. ASME Journal of Turbomachinery: 141(4), 01. 041001.

[22] Steinthorsson, E., Liou. M-S., and Povinelli, L., 1993, “Development of an Explicit Multiblock/Multigrid Flow Solver for Viscous Flows in Complex Geometries," Proceedings of the 29th Joint Propulsion Conference and Exhibit, AIAA Paper 1993-2380.

[23] Liou, M.-S., 2006, “A Sequel to AUSM, Part II: AUSM+-up for All Speeds," Journal of Computational Physics: 214, p 137-170.

[24] Kim, W.-W., and Menon, S., 1995, “A New Dynamic One-equation Subgrid-scale Model for Large Eddy Simulations," Proceedings of the 33rd AIAA Aerospace Sciences Meeting and Exhibit, January 1995, AIAA Paper 1995-356.

[25] Lilly, D. K., 1992, “A Proposed Modification of the Germano Subgrid-scale Closure Method", Physics of Fluids: 4, 633-635.

[26] Miki, K., and Ameri, A., "Large-Eddy Simulation of Variable Speed Power Turbine Cascade with Inflow Turbulence", ASME Journal of Turbomachinery: 143 (8): 081006.

[27] Miki, K., and Ameri, A., "Improved Prediction of Losses with Large Eddy Simulation in a Low-Pressure Turbine", ASME Journal of Turbomachinery: 144(7): 071002.

[28] Miki, K., and Ameri, A., "The Effect of Trailing Edge Grid Resolution in Large-Eddy Simulations", Proceedings of the ASME Turbo Expo, Gas Turbine Technical Congress and Exposition, no. GT2023-102276.

[29] Thurman, D., Flegel, A., and Giel, P., 2014, “Inlet Turbulence and Length Scale Measurements in a Large-Scale Transonic Turbine Cascade”, Proceedings of the 50th AIAA Joint Propulsion Conference, AIAA 2014-3934.

[30] Klein, M., Sadiki, A., and Janicka, J., 2003, “A Digital Filter Based Generation of Inflow Data for Spatially Developing Direct Numerical or Large Eddy Simulations", Journal of Computational Physics: 186, 652-665.

[31] Han, L. S. and Cox, W. R., 1982, “A Visual Study of Turbine Blade Pressure Side Boundary Layer”, Proceedings of the ASME 1982 International Gas Turbine Conference and Exhibit, London, UK, 18–22 April 1982; ASME paper 82-GT47.